Journal of Microscopy, Vol. 204, Pt 1, October 2001, pp. 69–86.
Received 18 February 2000; accepted 7 January 2001

A new sample preparation method for biological soft X-ray microscopy: nitrogen-based contrast and radiation tolerance properties of glycol methacrylate-embedded and sectioned tissue

B. W. LOO JR*, I. M. SAUERWALD†, A. P. HITCHCOCK‡ AND S. S. ROTHMAN§
**Bioengineering Graduate Group, University of California, San Francisco and Berkeley, School of Medicine, University of California, Davis, California, U.S.A.*
†Department of Growth and Development, University of California, San Francisco, U.S.A.
‡Brockhouse Institute for Materials Research, McMaster University, Hamilton, Ontario, L8S 4M1, Canada
§Departments of Physiology and Stomatology, University of California, San Francisco, Bioengineering Graduate Group, University of California, San Francisco and Berkeley, Genteric Corporation, Alameda, California, U.S.A.

Key words. Digital imaging microscopy, exocrine pancreas, glycol methacrylate tissue embedding and sectioning, microscopic protein mass measurement, nitrogen-based contrast, quantitative morphometry, radiation tolerance, sample preparation, synchrotron, transmission soft X-ray microscopy, XANES, zymogen granules.

Summary

We describe the preparation of a biological tissue for imaging in a transmission soft X-ray microscope. Sections of exocrine pancreas embedded in glycol methacrylate polymer, an embedding medium widely used in visible light and electron microscopy, were examined. Contrast was based primarily on the nitrogen content of the tissue, and dual-wavelength imaging at the nitrogen K-shell absorption edge was used to map the distribution and provide quantitative densitometry of both the protein and embedding matrix components of the sample. The measurements were calibrated by obtaining the absorption spectrum of protein near the nitrogen edge. The contrast was consistent and reproducible, making possible the first large-scale X-ray microscopic study on sections of plastic-embedded soft tissue. At radiation doses of up to 10^8 Gray, much more than required for routine imaging, no distortion and little mass loss were observed. This sample preparation method should permit routine imaging of tissues in X-ray microscopes, previously a difficult task, as well as multimodal imaging (using visible light, X-ray, electron, and scanned probe microscopies) on the same sample.

Correspondence: Billy W. Loo Jr MD PhD, Department of Radiation Oncology, Stanford University, Stanford, CA 94305, U.S.A. E-mail: BWLoo@mail.com

Introduction

Sample preparation technologies have been a cornerstone of traditional biological microscopy. Electron microscopy of biological samples would not have been possible without the development of myriad methods for fixing, embedding, sectioning, and staining or otherwise labelling cells and tissues. Likewise, biological visible light microscopy derives much, perhaps most, of its usefulness from such methods, even though in principle it can be and has been used to image living samples subjected to minimal preparation. This ability to image samples in a natural state is shared, and in a few aspects surpassed, by a relatively new form of microscopy that uses soft X-rays for illumination and X-ray optics for image formation (Schmahl *et al.*, 1980; Rothman *et al.*, 1990; Kirz *et al.*, 1995). Compared to electrons, soft X-rays penetrate much thicker samples, up to about 10 μm, or the full thickness of an unsectioned cell. Soft X-rays (typically of wavelength between 2 and 5 nm) interact with matter to produce high contrast biological images at atmospheric pressure based solely on intrinsic components rather than stains. By appropriate selection of illuminating wavelengths this contrast can be both element- and chemical-specific (Kenney *et al.*, 1985; Zhang *et al.*, 1996; Buckley *et al.*, 1998). Modern X-ray lenses, in the form of microfabricated diffractive optical elements called

zone plates (Anderson & Kern, 1992; Schmahl *et al.*, 1996; Weiß *et al.*, 1998), allow this to be accomplished at resolutions of 40–50 nm currently (Heck *et al.*, 1999), or about five times the resolution of visible light microscopes.

Perhaps because of these strengths, most of the work done in biological X-ray microscopy to date has concentrated on isolated cells and subcellular organelles or cultured cells grown in a single cell layer, often hydrated and sometimes initially living, imaged with little or no prior preparation. Nevertheless, the method stands to benefit greatly from the development of sample preparation techniques analogous to those used in visible light and electron microscopies, just as these other forms of microscopy have benefited. Currently, however, biological sample preparation for X-ray microscopy is an immature field, though a number of sample preparation methods are being developed, including immuno-labelling with silver enhanced gold beads (Larabell *et al.*, 2000; Meyer-Ilse *et al.*, 2000) or fluorescent probes (Irtel von Brenndorff *et al.*, 1994; Moronne, 1999) and cryogenic freezing (Maser *et al.*, 1998; Schneider & Niemann, 1998; Meyer-Ilse *et al.*, 2000).

One notable area of weakness has been the inability to image tissues in the X-ray microscope. Imaging tissues more than a few cell layers deep in any microscope requires sectioning them to a manageable thickness for the type of microscopy being used, because the illuminating radiation has a finite penetrating ability, and because the superposition of features from multiple depth layers in the sample makes structural interpretation difficult. In general, embedding tissue in some form of matrix is needed for sectioning, although with more limitations frozen, hydrated samples can be sectioned as well. Epoxy-embedded and sectioned mineralized samples such as bone, cartilage and calcified tendon have been imaged with element-specific contrast in an X-ray microscope (Kenney *et al.*, 1985; Buckley *et al.*, 1998). However, until recently, attempts to image soft tissues have had little success, apparently due to a lack of image contrast (C. J. Jacobsen, personal communication, 1999; P. Sicurello, personal communication, 1999). These attempts have included samples embedded in Epon and Epon/Araldite, with and without removal of the embedding medium before imaging. Nyakatura *et al.* (1988) obtained a single image of a section of rat kidney proximal tubule after removal of the Epon embedding medium by potassium hydroxide treatment. This image demonstrated good contrast and high-resolution features but the results were not reproducible (W. Meyer-Ilse, personal communication, 1999).

The problem with these previous attempts stems primarily from the difficulty of obtaining carbon-based contrast in samples consisting of organic materials embedded in a carbon-rich matrix. Recently, the authors and another group (Loo & Rothman, 1997; Khaleque & Buckley, 1998) have demonstrated satisfactory contrast in embedded and sectioned soft tissues. The latter work exploits contrast based on differences between protein and the embedding matrix in their near-edge absorption spectra at the carbon K-shell absorption edge. As discussed below, in the current work we take advantage of nitrogen-based contrast by using wavelengths shorter than the nitrogen K-shell absorption edge.

We describe here a method of embedding and sectioning a soft tissue that demonstrates a number of desirable features in an X-ray microscope, including high natural contrast and radiation tolerance. Glycol methacrylate (GMA, 2-hydroxyethyl methacrylate) polymer is a water-soluble plastic embedding medium used widely in visible light microscopy and, to a somewhat lesser extent, in electron microscopy. Several advantages of GMA embedding have been shown (Cole & Sykes, 1974; Bennett *et al.*, 1976): compared to paraffin, ultrastructural preservation and clarity are improved, tissue distortion is reduced, and thinner sections can be cut, from 0.5 to 3 μm routinely (ultrathin sections are also possible), with good uniformity of section thickness (Helander, 1983). Unlike epoxies, acrylic embedding media do not react covalently with tissue molecules; thus, plastic embedded tissue is still free to undergo specific labelling reactions with chemical reagents, enzymes or antibodies, making possible a wide range of histo- and immunochemistry (Bennett *et al.*, 1976; Brinn & Pickett, 1979).

Methods

Sample preparation

Pancreatic tissue was removed from the rat and fixed after a modification of the method of Ermak & Rothman (1981). Male Sprague–Dawley rats were fasted overnight for 18–22 h. They were anaesthetized by inhalation of methoxyflurane (Metofane, Mallinckrodt Veterinary, Inc., Mundelein, IN, U.S.A.), then sacrificed by decapitation and exsanguinated. The pancreas was removed and dissected into small pieces less than 1 mm in size. Tissue pieces were fixed in 1.5% glutaraldehyde and 1% paraformaldehyde in 0.08 M cacodylate buffer (pH 7.4) at 4 °C for approximately 24 h. They were then transferred to 0.08 M cacodylate buffer without the aldehyde fixatives, and stored at 4 °C for up to 21 days prior to embedding.

The embedding method was essentially a routine light microscopic preparation slightly modified from published protocols (Brinn & Pickett, 1979; Beckstead *et al.*, 1981) using the JB-4 embedding kit from Polysciences, Inc. (Warrington, PA, U.S.A.), a formulation of the GMA embedding technique. Tissue pieces were dehydrated by immersion in 70% acetone (diluted with water) for 15 min,

followed by four exchanges of 100% acetone at 20 min each. They were then infiltrated by immersion in a 1 : 1 mixture of acetone and JB-4 Solution A, primarily consisting of GMA monomer with some of the plasticizer n-butoxyethanol (two exchanges at 30 min each), followed by 100% JB-4 Solution A overnight at 4 °C under vacuum. All the reagents for the dehydration and infiltration steps were used cold (4 °C). Prior to polymerization the tissue pieces were transferred to catalysed Solution A (0.18 gram catalyst, containing benzoyl peroxide, per 40 mL Solution A) for 1 h. They were then placed in polyethylene block moulds with 6 × 8 × 5 mm octagonal wells, covered with freshly prepared polymerizing mixture (40 : 1 mixture of catalysed Solution A to Solution B, containing the accelerator N,N-dimethylaniline) and plastic block holders, and allowed to polymerize overnight. Again, these steps were carried out at 4 °C, and under vacuum to prevent atmospheric oxygen from inhibiting the polymerization.

The blocks were sectioned with glass knives using a Reichert-Jung (Leica) 2050 Supercut automatic rotary microtome. Sections nominally 0.75 μm thick were cut dry and transferred with forceps to a clean water bath at room temperature where they flattened by surface tension. They were then picked up on sample holders and air dried at room temperature. No mounting medium or coverslip was used, leaving the sample exposed on one side. The sample holder used in this study consisted of a square silicon wafer frame, 100 μm thick and 11 mm wide, supporting a membrane of X-ray transparent silicon nitride 100 nm thick over a 3.5-mm square hole (window) in the centre of the wafer. The sample holders were fabricated by lithographic techniques at Lawrence Livermore National Laboratory by Dino R. Ciarlo.

The X-ray microscope

We used a transmission soft X-ray microscope, called XM-1 (Meyer-Ilse *et al.*, 1995; Meyer-Ilse *et al.*, 1998), at the Advanced Light Source (ALS), a high-brightness synchrotron radiation facility at Lawrence Berkeley National Laboratory (LBNL). XM-1 is a conventional-type, or full-field imaging, microscope. Figure 1 is a schematic representation of the optical layout. The microscope uses two zone plates as lenses, one as a condenser that demagnifies the incoherent light source (a bending magnet on the ALS) onto the sample, and the other as an objective that images the sample onto a detector. The detector is a charge-coupled device (CCD) camera, thinned and back-illuminated for high efficiency detection of soft X-rays (Wilhein *et al.*, 1994). The digital output of the camera is read directly into a computer for storage and subsequent processing.

Zone plates have strong axial chromatic aberration. As a result, the condenser zone plate also serves as a monochromator (Niemann *et al.*, 1983), in conjunction with a pinhole just upstream of the sample plane, and provides a spectral resolution ($\lambda/\Delta\lambda$) of 300, or a bandwidth of about 0.01 nm in the wavelength range used. This allows wavelength tuning over the broad emission spectrum of the source. The wavelengths used in this study were 2.4 nm, just below the oxygen K-shell absorption edge in energy (the low absorption side), and 3.1 and 3.0 nm, on either side of the nitrogen K-shell absorption edge.

This X-ray microscope employs a unique sample mounting and positioning system, with two separate sample stages, one each in the X-ray microscope and an external visible light microscope (VLM). The sample mounts reproducibly to either stage via a magnetic kinematic mounting system, and the coordinate systems of the two

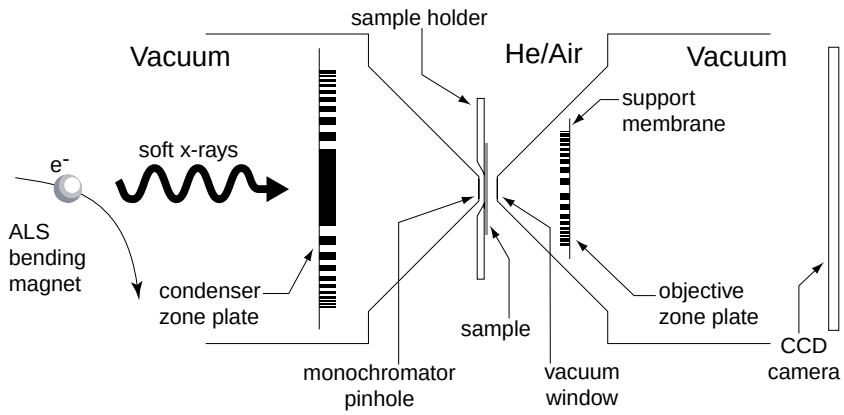

Fig. 1. Schematic representation of the optical layout of the high-resolution X-ray microscope XM-1. The design is of the conventional, full-field imaging type. The optical elements are in vacuum, and the vacuum windows (one of which serves as a monochromator pinhole) are mounted on cones close to the sample to minimize the air gap surrounding the sample, where the remaining air is largely displaced by a stream of helium gas. The optical efficiency of all elements downstream of the sample (the helium/air gap, vacuum window, zone plate lens and support membrane, and CCD camera) affects the dose required to form an image of a given statistical quality.

stages are related by a known correspondence. It is therefore possible to do all sample selection and focusing using the VLM, with no X-ray exposure prior to final imaging.

Images were acquired in one of two modes: single field or montage. The image field size of XM-1 in its standard configuration is a circular area of about 8–10 μm depending on the magnification (usually 2400 times). To expand the field size an algorithm was developed to assemble large-field image montages from many standard-size subfields (Loo *et al.*, 2000). Most of the images in this study were acquired in this mode.

Measurement of radiation tolerance

Radiation tolerance measurements were performed on a sample prepared as described above at 2.4 nm wavelength (the usual operating wavelength in this instrument). Ten image fields of pancreatic tissue were selected using the VLM and were imaged 2, 4, 6, 8 or 10 times at an exposure level sufficient to produce a good quality image in terms of photon counting statistics. A super-region encompassing the 10 exposed subfields was then selected and imaged by assembling a montage (see Fig. 3a) to demonstrate any potential change in the exposed areas relative to their surroundings. In addition, several fields in bare GMA plastic portions of the section, containing no pancreatic tissue, were exposed multiple times at 3.0 nm or 3.1 nm wavelength, or both, and the change in mass measured. Finally, a large-field montage image was acquired at 2.4 nm wavelength of an area containing smaller fields previously imaged at a very high dose at 3.0 and 3.1 nm wavelength (see Figs 5 and 6).

Calculation of dose

Dose is absorbed energy per unit mass, measured in Gray (joules kg^{-1}). Both the absorbed energy and the mass of the sample are calculated quantities, derived from the measurement of photons detected by the CCD camera. Images are acquired of both the sample and a background region on the sample holder window where no sample is present. The ratio of these images gives the transmissivity T (fractional energy transmission) of the sample (on a pixel by pixel basis):

$$T = \frac{I}{I_0} \cdot \frac{e_0}{e} \tag{1a}$$

where I is the detected signal intensity through the sample, I_0 is the detected intensity through the background region, and e and e_0 are the corresponding exposure levels (product of exposure time and synchrotron beam current) at which the images were recorded. I and I_0 are corrected for dark current in the CCD detector. The transmissivity is also related to the physical properties of the sample by (Henke *et al.*, 1993):

$$T = \exp(-\mu\rho_a) \tag{1b}$$

where μ is the mass-dependent absorption coefficient for the sample material, and ρ_a is its areal density (mass per unit area perpendicular to the X-ray beam or optical axis).

Given these relationships, we can determine the quantities of interest. The absorbed energy A (the portion that is not transmitted) is:

$$A = (T^{-1} - 1)\cdot I \cdot Q^{-1} \tag{2}$$

where Q is the light transfer/detection efficiency of all components in the optical path downstream of the sample (see Fig. 1). The mass M of the sample (per pixel) is given by:

$$M = a\rho_a = -\frac{a}{\mu}\log T \tag{3}$$

where a is the area of a pixel. Dose is then the ratio of A to M.

The two quantities that must be known or approximated to calculate the dose from the measured transmissivity T are μ and Q. The mass-dependent absorption coefficients (μ) for the elements have been tabulated at wavelengths from 0.04 to 122 nm (Henke *et al.*, 1993). If the relative proportions of elements in a material are known, the composite absorption coefficient for the material can be calculated from the tabulated values. The absolute molecular formula is not required. The composition of GMA polymer was taken to be $C_6H_{10}O_3$ (Bennett *et al.*, 1976), and the composition of protein was taken to be $C_{100}H_{155}N_{27}O_{30}S$. The formula for protein was derived by examining the primary sequences of several proteins (available in the *Entrez* online database from the National Center for Biotechnology Information, National Institutes of Health, http://www.ncbi.nlm.nih.gov) found in the pancreas or mammalian tissues (amylase, trypsinogen, lipase, collagen and albumin), and taking the average composition assuming no glycosylation. The calculated absorption coefficient for this generic protein formula is within 1% of those of the individual proteins listed above over the wavelength range used, indicating little variation in absorbance from one protein to another.

The light transfer efficiency Q is a product of the transmissivity of the narrow gas-filled gap between the sample and the vacuum window, the transmissivity of two silicon nitride windows (the vacuum window and the support membrane for the objective zone plate) totalling 225 nm in thickness, the diffraction efficiency of the objective zone plate, and the quantum efficiency of the CCD camera. Given the elemental composition and density of a material, its transmissivity can be calculated from the tabulated absorption coefficients and Eq. (1b). During imaging, a stream of helium gas (which absorbs X-rays very weakly) flows around the sample, displacing nearly all of the atmospheric air in its vicinity (which can absorb

strongly depending on the wavelength due to its high nitrogen content). Assuming a 99% displacement of air, the helium/air gap transmits over 99% of the X-rays emerging from the sample. The silicon nitride windows together transmit 39, 20 and 40% at wavelengths of 2.4, 3.0 and 3.1 nm, respectively. The calculated (theoretical) diffraction efficiency of the zone plate used in this experiment was 5%, and the actual efficiency was probably about 3%. The quantum efficiency of the same type of CCD as used in this instrument has been measured (Wilhein *et al.*, 1994), and is between 55 and 65% over the wavelength range used. Thus, the overall light transfer efficiency was between 0.36 and 0.74%, depending on the wavelength. Not accounted for was absorption due to deposition of a carbon contaminant on the objective zone plate because of poor vacuum at the time of this experiment. The contamination increased gradually with X-ray exposure, and caused an additional variable amount ($< 50\%$) of absorption over the course of these measurements. Overall, taking these uncertainties into account, the dose estimates presented here are probably accurate to within a factor of 2–4, and are probably underestimates.

Calculation of protein and plastic content

Most of the images in this study were acquired at 2.4 nm wavelength, the usual operating wavelength of the XM-1 instrument. In order to calibrate these images for quantitative protein measurements, two sample areas were imaged at wavelengths on both sides of the nitrogen K-shell absorption edge. Let us assume for the moment that the sample consists solely of two materials, m_1 and m_2, and that at each of two wavelengths, λ' and λ'', the corresponding absorption coefficients, μ_1', μ_1'', μ_2' and μ_2'', are known. Then by Eq. (1b):

$$\begin{aligned} \mu_1'\rho_{a,1} + \mu_2'\rho_{a,2} &= -\log T' \\ \mu_1''\rho_{a,1} + \mu_2''\rho_{a,2} &= -\log T'' \end{aligned} \tag{4}$$

Two measurements, T' and T'', make it possible to solve for the two unknowns, $\rho_{a,1}$ and $\rho_{a,2}$ (the areal densities of the two component materials), as follows:

$$\rho_{a,1} = \frac{-\mu_2''\log T' + \mu_2'\log T''}{\mu_1'\mu_2'' - \mu_1''\mu_2'}$$

and

$$\rho_{a,2} = \frac{\mu_1''\log T' - \mu_1'\log T''}{\mu_1'\mu_2'' - \mu_1''\mu_2'} \tag{5a}$$

or rearranged,

$$\rho_{a,1} = \frac{-\log T' + \left(\frac{\mu_2'}{\mu_2''}\right)\log T''}{\mu_1' - \mu_1''\left(\frac{\mu_2'}{\mu_2''}\right)}$$

and

$$\rho_{a,2} = \frac{-\log T' + \left(\frac{\mu_1'}{\mu_1''}\right)\log T''}{\mu_2' - \mu_2''\left(\frac{\mu_1'}{\mu_1''}\right)} \tag{5b}$$

This system of equations is ill-conditioned (i.e. produces an unstable solution) if the absolute value of its determinant $|\mu_1'\mu_2'' - \mu_1''\mu_2'|$ is small. The imaging wavelengths λ' and λ'' should therefore be chosen to maximize this quantity. For example, if they are on either side of an absorption edge of one of the components, e.g. m_1, the absorption coefficient μ_1 will have a large change across the edge, with little change in μ_2, resulting in a determinant of large magnitude.

To a good approximation, a soft tissue sample prepared as described above consists entirely of organic molecules such as protein, nucleic acids, lipids, and the plastic embedding medium. These molecules contain varying proportions of the elements carbon, hydrogen, nitrogen, oxygen, phosphorus and sulphur. Protein and nucleic acids can be distinguished from the other constituents (the plastic matrix being of greatest concern) by their high nitrogen content (16–17% by mass).

As a consequence, we can model the sample as having two components: nitrogen (assigned to m_1) and a composite material consisting of the rest of the elements in the sample (assigned to m_2). The two chosen wavelengths (3.0 and 3.1 nm) straddle the nitrogen K-shell absorption edge (nominally 3.025 nm). The attenuation coefficients of GMA polymer and the non-nitrogenous part of protein are sufficiently different from each other that we cannot assume a single value for μ_2' or μ_2''. However, as apparent in Eq. (5b), to determine the nitrogen mass only the ratio of μ_2' to μ_2'' is required, and this ratio is constant to within 0.1% for the materials of interest (GMA polymer, non-nitrogenous parts of protein and DNA, lipids, carbohydrates), with a value of 0.92 for the two given wavelengths. The protein and DNA mass can then be calculated based on their known fractional nitrogen content, and the balance of the mass, if assumed to be due to GMA polymer, can subsequently be calculated given the measured transmissivities by Eq. (4).

We applied two additional corrections in our calculations. First, we attempted to account for possible errors due to radiation exposure effects. The two sample areas selected for nitrogen edge imaging in this experiment were the central regions of two pancreatic acini (see Figs 5 and 6). In order to allow for the correction of possible changes in transmissivity due to radiation-induced mass loss, one acinus was imaged at 3.1 nm first followed by 3.0 nm, and the other was imaged in the reverse wavelength order. The first image of each pair (having received no prior radiation dose) could then serve as a control for the second of the other pair. Pixels in three intensity ranges were selected in each of

the image pairs corresponding to high protein density (in the middle of the dense zymogen granules), intermediate protein density (in cytoplasmic regions between granules) and low protein density (in the duct lumen). A linear transformation was applied to the transmissivity values in the second image of each pair to make pixel values in each of the intensity categories more similar to those in the corresponding intensity categories in the first image of the opposite pair. Calculations were then performed on the corrected images as described above. Attempting in addition to correct the first image of each pair for the dose deposited in that first exposure using the mass loss curves described below (see Fig. 4) had a negligible impact on the results.

Second, the wavelengths used were sufficiently close to the nitrogen absorption edge that near-edge effects due to covalent bonding and other environmental factors cause a substantial deviation of the absorption coefficient of nitrogen from its tabulated theoretical values. We estimated the true absorption coefficients by measuring the absorption spectrum of a protein (albumin) near the nitrogen edge as described in the next section. These were the values used for μ_1 in the above relationships to determine the mass of protein and plastic.

XANES spectrum of albumin, and the determination of the mass-dependent absorption coefficient in the nitrogen K-shell region

Equation (5) above in principle allows the determination of the nitrogen content of a sample given two images acquired using X-ray wavelengths on either side of the nitrogen K-shell absorption edge. Required in these expressions are the mass-dependent absorption coefficients at each of the two wavelengths, for each of the two components of the sample's mass: that due to nitrogen, and that due to all other elements in the sample. As already noted, although the absorption coefficients have been tabulated for all the elements over a wide range of wavelengths (Henke *et al.*, 1993), the true coefficient for an element deviates substantially from the tabulated values at wavelengths near its absorption edges. This X-ray absorption near-edge structure (XANES) in the spectrum of an element is strongly influenced by the local environment of the atom, particularly covalent bonds to adjacent atoms. For nitrogen in protein, the amide bond has the greatest influence on the spectrum near the nitrogen edge.

To obtain accurate absorption coefficients for nitrogen in protein, we determined the spectrum of a protein, albumin, near the nitrogen edge, using the spherical grating beamline (Yates *et al.*, 2000) operated by the Canadian Synchrotron Radiation Facility at the Synchrotron Radiation Centre of the University of Wisconsin, Madison. The sample was deposited from solution onto a metal plate cleaned by acid etching and the relative absorption spectrum was recorded using total electron yield as detected by the sample current. We obtained the spectrum of albumin near the carbon K-edge as well. In other work, the nitrogen K-shell spectrum of albumin, along with the carbon K-shell spectra of albumin and fibrinogen, are being used as standards for investigations of the localization of these proteins on polymer surfaces (Hitchcock *et al.*, 2000) using the scanning transmission X-ray microscope (STXM) on beamline 7.0.1 (an undulator beamline) of the Advanced Light Source at LBNL (Warwick *et al.*, 1998). Similar XANES spectra of proteins have been measured by others at the nitrogen edge (Kirtley *et al.*, 1992; Shinohara *et al.*, 1998; Ito *et al.*, 2000) and the carbon edge (Zhang *et al.*, 1996), but were not converted to mass-dependent absorption coefficients.

The mass-dependent absorption coefficient of albumin is directly proportional to the relative absorption spectrum obtained by the total electron yield measurement. We determined the proportionality constant by first assuming that the regions of the spectrum far from the absorption edges coincide with the tabulated theoretical values. The molecular formula for bovine serum albumin is $C_{3071}H_{4826}N_{816}O_{927}S_{40}$, based on its primary structure and assuming no glycosylation (data from the *Entrez* online database, http://www.ncbi.nlm.nih.gov). The theoretical mass-dependent absorption coefficient based on this formula for albumin is plotted in Fig. 2. For the theoretical spectrum, the edge transition energies were set to 405 eV (for the nitrogen K-edge) and 292 eV (carbon K-edge), which are values estimated by comparing the spectral features of albumin with those of amide molecules for which the ionization limits are known (Hitchcock & Mancini, 1994).

We wish to find the proportionality constant k that minimizes the difference D in a least squares sense between the measured and theoretical values at the tail ends of the spectrum:

$$D = \sum_i \mu_{tab,i} - k \cdot OD_i)^2 \qquad (6)$$

where μ_{tab} are the tabulated coefficients, OD are the measured optical densities based on total electron yield, and i is the index over the 20 data points at each end of the measured spectrum. The value of k that minimizes D is:

$$k = \frac{\sum_i \mu_{tab,i} \cdot OD_i}{\sum_i OD_i^2} \qquad (7)$$

The measured spectrum, $\mu_{meas} = k \cdot OD$, is also plotted in Fig. 2. It can be seen from the figure that at the tail ends of the measured spectra, where they are expected to coincide with the theoretical ones, the agreement is not exact. This might be because the range of wavelengths sampled was insufficient to reach the limit of purely elemental rather

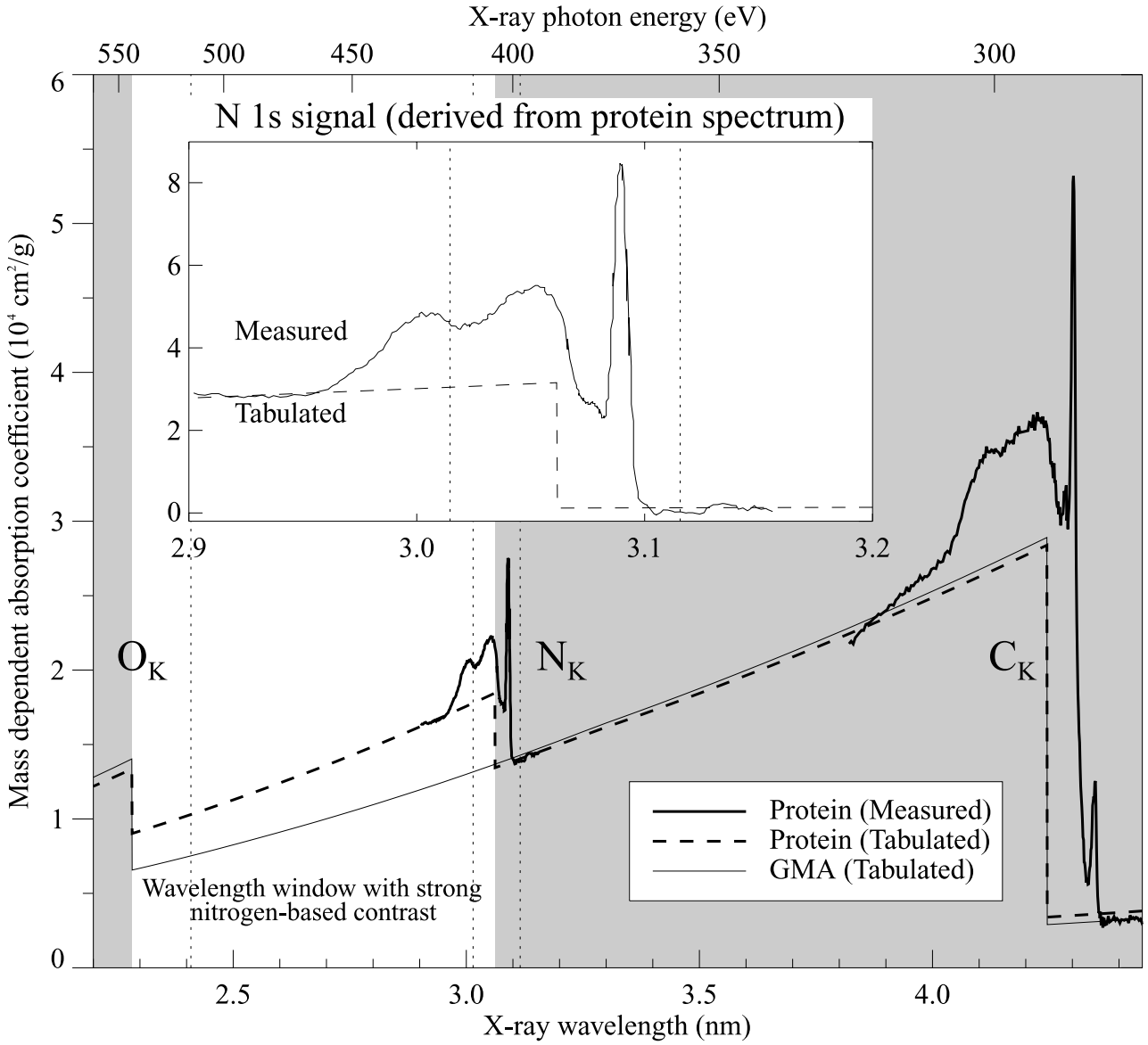

Fig. 2. Mass-dependent absorption coefficient spectra of a protein (albumin) and glycol methacrylate (GMA). For albumin, both the tabulated theoretical values based on its elemental composition and the measured values near the nitrogen and carbon K-shell absorption edges are plotted. The tabulated and measured values differ substantially due to near-edge spectral features, which are sensitive to molecular structure. In the wavelength window between the oxygen and nitrogen absorption edges, the difference between the absorption coefficients of protein and GMA due to the nitrogen content of protein provides most of the contrast in images acquired at these wavelengths, whereas outside this wavelength range, their spectra nearly coincide. Dotted lines indicate the wavelengths used in this study, nominally 2.4, 3.0 and 3.1 nm, but with corrections for miscalibration. Inset, the mass-dependent absorption coefficient spectrum of nitrogen in protein derived from the measurements on albumin, compared to the tabulated values. In effect, this represents the spectral character of elemental nitrogen in the environment of a protein molecule (albumin).

than molecular spectral character (Hitchcock & Mancini, 1994), or due to another systematic error such as that caused by stray light in the system.

At wavelengths near the nitrogen edge, the difference between the measured albumin absorption spectrum and the theoretical spectrum based on its elemental composition is due to its nitrogen K-shell near-edge features. The contributions of the nitrogen and non-nitrogen components can be separated as:

$$\mu_{meas} = f_N \mu_N + (1 - f_N)\mu_{other} \tag{8a}$$

where μ_{meas} is the measured absorption coefficient of

albumin as above, μ_N is absorption coefficient of the nitrogen component, μ_{other} is the absorption coefficient of the non-nitrogen component, and f_N is the fraction of the molecular weight of albumin due to nitrogen. This gives:

$$\mu_N = \frac{\mu_{meas} - (1 - f_N)\mu_{other}}{f_N} \tag{8b}$$

f_N is 16.5% for albumin. μ_{other} is taken to be the theoretical values based on the tabulated data for a compound with the formula $C_{3071}H_{4826}O_{927}S_{40}$ (albumin without the nitrogen component). The actual values for the absorption coefficient of the nitrogen component derived in this way are plotted in Fig. 2 (inset), along with the tabulated values. This can be interpreted as the spectral character of elemental nitrogen in the environment of a protein molecule (albumin).

Also indicated in Fig. 2 are the two wavelengths used in the dual-wavelength imaging portion of this study. The energy scale of the N 1s spectrum of albumin acquired by total yield was calibrated against the well characterized 3s and 3p Rydberg peaks of nitrogen gas (N_2) (Chen *et al.*, 1989), and is accurate to within 0.05 eV. However, there was an energy calibration error in XM-1 estimated at approximately 2 eV in energy or 0.015 nm in wavelength, based on the transmission spectrum of the silicon nitride windows. Thus, while the nominal wavelengths used were 3.0 and 3.1 nm, the actual wavelengths were 3.015 and 3.116 nm. At 3.015 nm wavelength the measured absorption coefficient of the nitrogen component was 4.6×10^4 cm^2 g^{-1} while the corresponding tabulated value for elemental nitrogen is 3.1×10^4 cm^2 g^{-1} (see inset to Fig. 2). At 3.116 nm wavelength the measured and tabulated values were nearly the same at 1.3×10^3 cm^2 g^{-1}. As can be seen from Eq. (5), using the tabulated values would have resulted in calculated nitrogen or protein densities that are too large by about 40%.

Results and discussion

Contrast

Figure 3(a) is an image montage acquired at 2.4 nm wavelength. It demonstrates unambiguously many structural and ultrastructural features at high resolution. These include capillary endothelial cells (C), numerous pancreatic exocrine cells arranged in clusters called acini (A), cell nuclei (N), nucleoli (n), mitochondria (m) and zymogen granules (zg). In addition, the nucleus of a centroacinar cell (ca) is visible in one of the acini. The contrast evident in this image was consistently achievable for all the samples in this study, which included sections from multiple pancreatic tissue pieces from each of seven animals. Nearly 100 large-field montages like this one were acquired, consisting of nearly 27 000 individual subimages, making this the largest X-ray microscopic study to date. This work was part of a larger experiment in which we set out to measure the population statistics on size, protein mass and number of zymogen granules in pancreatic exocrine tissue to evaluate mechanisms of protein transport (Rothman *et al.*, 1992; Loo *et al.*, 1996). The biological results will be published in a separate paper.

A useful image can be recorded only if there is a difference in the absorption of X-rays between sample features, consisting primarily of protein or nucleic acid, and their background, the plastic embedding matrix in this case. Figure 2 contains a plot of the mass-dependent absorption coefficients of protein and GMA polymer over a range of wavelengths including the carbon, nitrogen and oxygen K-shell absorption edges. Clearly, at wavelengths between the nitrogen and oxygen edges (including the 2.4 and 3.0 nm wavelengths used in this study) a sample pixel filled with protein would absorb X-rays significantly more strongly than a pixel containing the same mass of plastic. Conversely, the same two pixels would be difficult to distinguish if illuminated by X-rays with a wavelength longer than the nitrogen edge or shorter than the oxygen edge. Thus, nitrogen content is the main contributor to image contrast.

All previous work on embedded and sectioned soft tissue has been done with X-ray wavelengths longer than that at the nitrogen edge. This probably accounts for much of the difficulty in obtaining satisfactory contrast. Contrast was nevertheless seen in sections of embedded mineralized tissues probably because unlike soft tissues, which are composed mainly of water (that subsequently is replaced by the embedding material), such tissues are composed primarily of dense material with little water content, and thus give appreciable contrast against the embedding matrix based on density alone. The X-ray microscope that was used for almost all of this earlier work, the Stony Brook scanning transmission X-ray microscope (STXM) at the National Synchrotron Light Source at Brookhaven National Laboratory (Kirz *et al.*, 1995; Maser *et al.*, 1998), has a longer portion of the optical path in air, so that absorption due to atmospheric nitrogen made using shorter wavelengths, like those used in this work, unfavourable (C. Jacobsen, personal communication, 1999). On the other hand, in XM-1 the monochromator pinhole and downstream vacuum window are mounted on cones that can be positioned very close to the sample, minimizing the air gap. This helps overcome the problem, and in fact 2.4 nm is the usual operating wavelength of the microscope.

Recently, Khaleque & Buckley (1998) used a wavelength at which the embedding materials have stronger absorbance than protein, producing negative contrast. This is due to near-edge effects at the carbon edge. Similarly, as seen in Fig. 2, at another wavelength near the carbon edge (4.35 nm) protein has a relatively strong near-edge

absorption peak due to its aromatic content that could, in principle, be exploited to produce contrast because the plastic has a low aromatic content. Our main objective, however, beyond obtaining high contrast images, was to do quantitative imaging, i.e. to obtain meaningful numbers from our measurements, and there are some practical barriers to using such wavelengths for that purpose. First, taking advantage of sharp spectral features requires a more accurate wavelength calibration than was available in our instrument at the time. Second, even with good calibration, finite spectral bandwidth and finite sample thickness result in beam hardening effects that make it difficult to measure absorption coefficients accurately near sharp features. Third, because of the large number of carbon-containing chemical species in the sample, the two-component sample model we used would probably be inadequate when imaging with wavelengths near the carbon edge. The ability to use wavelengths shorter than the nitrogen edge (currently being incorporated in the Stony Brook STXM as well) has the advantage of strong contrast due to the high content of nitrogen in protein and nucleic acids and its absence in the plastic, and also helps avoid some of these ambiguities. Alternatively, some of these difficulties could be overcome by spectromicroscopy, or imaging at many closely spaced wavelengths (Zhang *et al.*, 1996; Ade *et al.*, 1997), at the cost of increased experimental complexity. We have also initiated experiments using this approach. Yet another method that might be used to obtain similar information is electron microscopic electron energy loss spectroscopy (EELS) (Leapman & Andrews, 1991). This method provides higher resolution at the cost of increased radiation damage, particularly when near-edge spectral features are used (Rightor *et al.*, 1997).

Radiation tolerance

Indicated on Fig. 3(a) are 10 subfields that were imaged two to 10 times prior to acquisition of the large-field montage. Only in the most heavily exposed (10 times) fields is a change in intensity appreciable visually, and only then because the intensity scale of the display has been adjusted to emphasize the difference. Figure 3(b) shows the central part of each of these areas displayed as a ratio of the first exposure to the last. Darker pixels indicate a greater change in transmissivity. Several features are notable in these images. First, the degree of change in transmissivity (due to mass loss) is dose dependent. Second, it is non-uniform, being greater in areas of lower protein density. Third, despite the mass loss, there is no discernable distortion of the sample after up to 10 exposures. Distortion would manifest as misalignment of the edges of features in these ratio images, resulting in ghosting.

Figure 4 shows plots of sample mass, expressed as a fraction of the initial mass, vs. dose. The mass axis is a log scale. A straight line would be expected if a fixed fractional mass loss were produced by each increment in dose. The data fall on a curve, however, suggesting a biphasic or multiphasic response to dose, with decreasing fractional mass loss per unit dose at higher doses. The fitted curves shown are quadratic functions. The data from the images in Fig. 3(b) are plotted as four curves. One results from averaging pixel values over each of the individual exposures. The other three result from partitioning the pixels into three categories: high protein density (in the middle of the dense zymogen granules), intermediate protein density (in cytoplasmic regions outside granules), and low protein density (in extracellular areas). The slope, or extent of mass loss with dose, is least in high protein density areas. The last curve was generated from data on bare GMA plastic areas exposed multiple times at 3.0 or 3.1 nm wavelength. The slope is similar to that of the low protein density curve at 2.4 nm wavelength. These observations suggest that the GMA component of the sample is significantly more sensitive to radiation than the protein component, and that the dose sensitivity is approximately independent of wavelength (at least for the plastic matrix).

A dose of 1.2×10^7 Gray (Gy) produces a 5% mass loss in plain GMA polymer, as do 4.4×10^7 Gy and 6.8×10^7 Gy in areas of intermediate and high protein density, respectively. In tissue on the whole, it takes 3.5×10^7 Gy to produce a 5% mass loss, and even at 10^8 Gy mass loss is less than 10%. On the other hand, the dose used to form a single image, with all the above-mentioned inefficiencies in the system at the time, was about 10^7 Gy at 2.4 nm, 5×10^7 Gy at 3.0 nm, and 2×10^7 Gy at 3.1 nm. Thus, the potential mass loss at the nitrogen edge was non-negligible and corrections were needed to compensate for radiation effects, while imaging at 2.4 nm wavelength produced relatively minimal changes.

Figure 5 demonstrates the mass loss that occurs with extremely high doses. It is a large field montage (at 2.4 nm wavelength) encompassing two smaller areas that were also imaged earlier in montage mode at both 3.0 and 3.1 nm wavelength. The prior cumulative dose to these areas was about 7×10^9 Gy. The fractional mass loss was 19% in high protein density areas, 25% in intermediate protein density areas, and 31% in low protein density areas. Based on the curves in Fig. 4, these appear to be practically asymptotic values for mass loss. Furthermore, despite the significant mass loss there appears to be no appreciable distortion of basic cellular and tissue architecture.

Although the samples were sufficiently robust to tolerate these doses, minimizing dose is clearly desirable. Even in a single exposure, the doses used were far higher than theoretically required to produce images of equivalent quality. The main reason for this is the low light transfer efficiency of all the components downstream of the sample (significantly less than 1%, as described above in Methods),

the largest loss being in the objective zone plate. Methods are being developed to produce zone plates with substantially better diffraction efficiency (Weiß *et al.*, 1998; Anderson, 2000). In addition, a much greater reduction in dose is possible using a scanning microscope, in which a single zone plate is used to form an X-ray microprobe that is scanned across the sample. Only the detector is downstream of the sample in this case, and compared to the current work, the required dose should be roughly two orders of magnitude lower.

There was another source of inefficiency in montage mode imaging at the time of this study. The available monochromator pinhole was a 15 μm square hole. Because the monochromator pinhole defines the size of the irradiated area on the sample, a larger area was exposed than fit within the imaged area (the 8–10 μm circular field of view). Consequently, most of the subfields imaged in montage mode (except those at the edges of the superregion) received the equivalent of about four exposures (when images of some of their neighbouring subfields were

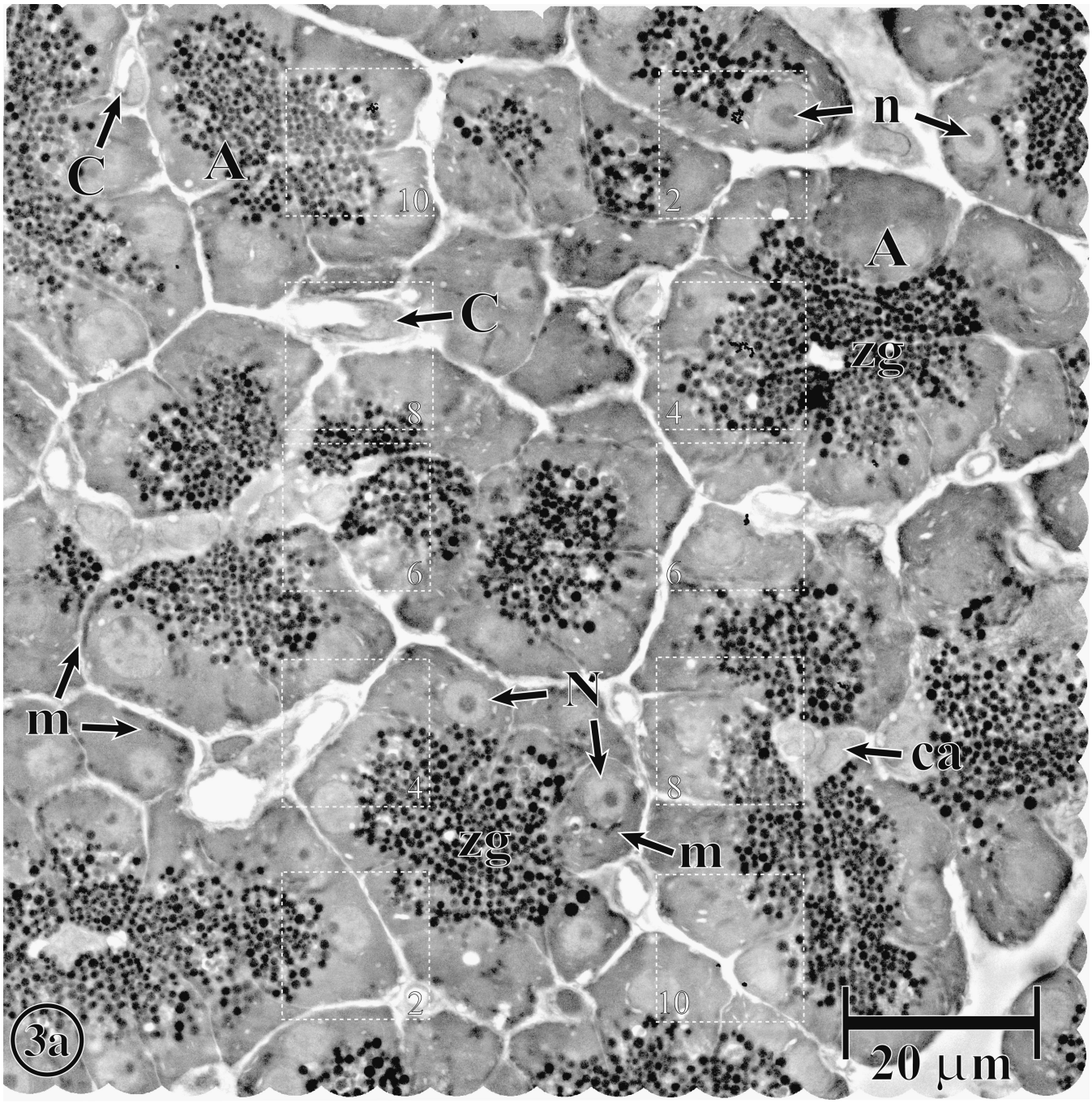

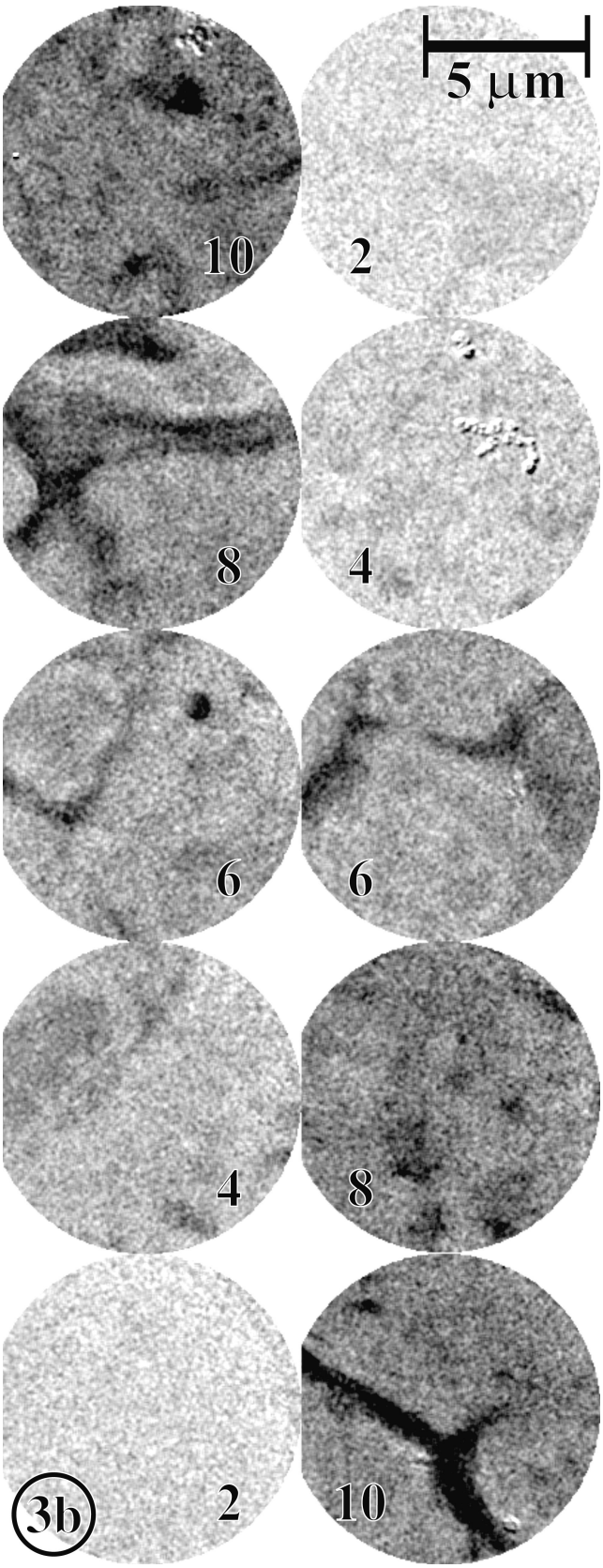

acquired) before actually being imaged themselves. Furthermore, by the end of a montage acquisition sequence, most of the imaged area was exposed about nine times. Single field imaging at a spacing greater than the monochromator pinhole size is not affected. A smaller monochromator pinhole has subsequently been installed, allowing montage image acquisition with a dose similar to that in single image mode (in addition to improving spectral resolution).

Finally, as to the mechanism of mass loss with soft X-ray exposure in dry samples such as these, it must involve volatilization or vaporization of the sample. This might happen by reaction with residual atmospheric oxygen not displaced by helium (or ozone produced by its ionization by X-rays). An observation consistent with this hypothesis is that visible light fluorescence (observed in a visible light microscope) increases in an area of formaldehyde-fixed cultured cells after it is imaged in the X-ray microscope (W. Meyer-Ilse, personal communication, 1999). Enhancement of fluorescence in formaldehyde-fixed samples by exposure to ozone is a known technique in histochemistry (Pearse, 1985). If reaction with atmospheric oxygen is in fact the mechanism of mass loss, it should be possible to prevent or at least reduce mass loss by excluding air around the sample more completely, for example by building a helium filled chamber around the sample stage.

Distribution of protein and GMA polymer

Figure 6 shows two image fields in the centres of two acini at both 3.0 and 3.1 nm wavelength (a) and (b), their calculated nitrogen mass distribution (c), and calculated GMA polymer distribution (d). The high, intermediate and low protein density regions had average protein areal densities of

Fig. 3. (a) An image montage acquired at 2.4 nm wavelength of GMA-embedded and sectioned pancreatic tissue, demonstrating many structural and ultrastructural features at high resolution and with strong contrast. Clearly visible are pancreatic exocrine cells arranged in clusters called acini (A), cell nuclei (N), nucleoli (n), mitochondria (m), many protein-rich zymogen granules (zg) surrounding ductal spaces at the centre of the acini, capillary endothelial cells (C), and the nucleus of a centroacinar cell (ca) in one of the acini. The total image size is about 2700 × 2700 40 nm pixels, or a little over 100 × 100 μm in area. The 10 regions marked by squares were each imaged the specified number of times prior to acquiring the large field montage to measure the extent of radiation induced mass loss. Only in the most heavily exposed fields (10 times) is an intensity difference visually appreciable, even with the intensity scale adjusted to emphasize the difference. (b) The ratio of the first exposure to the last, in the central part of each of the pre-exposed areas in (a). Areas with the greatest change in transmissivity between the first and last exposures appear the darkest, demonstrating a dose-dependent mass loss that is also spatially non-uniform, with greater loss in areas of lower protein density.

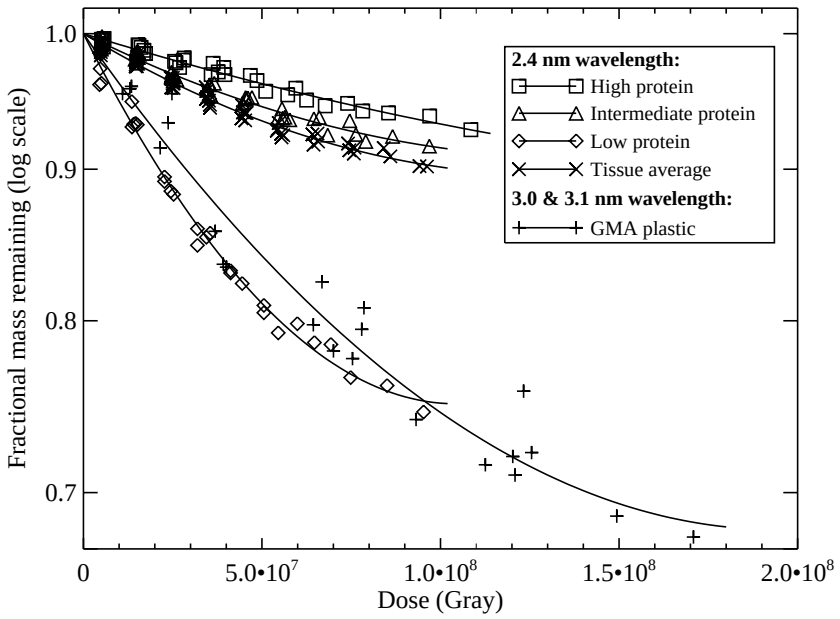

Fig. 4. Plots of sample mass remaining vs. dose. The data at 2.4 nm wavelength are from the measurements from Fig. 3. Even at doses of 10^8 Gy, there is a less than 10% mass loss in tissue as a whole, while the dose required to form an image of good statistical quality in this study was only about 10^7 Gy (which because of optical inefficiencies was itself over 100 times greater than the theoretically required dose). The GMA plastic component of the sample appears significantly more radiation sensitive than the protein component, and this sensitivity is similar across the wavelengths used.

6.9×10^{-5}, 3.9×10^{-5} and 2.8×10^{-5} g cm^{-2}, respectively, and average GMA polymer areal densities of -0.1×10^{-5}, 2.3×10^{-5} and 2.6×10^{-5} g cm^{-2}, respectively. Based on the transmissivity of pure GMA regions in the sample, the thickness of the section was estimated (as described in the next section) to be 0.51 μm. This allows an estimation of volumetric density (as areal density divided by thickness), yielding high, intermediate, and low average protein densities of 1.36, 0.77 and 0.56 g cm^{-3}, respectively, and corresponding average GMA

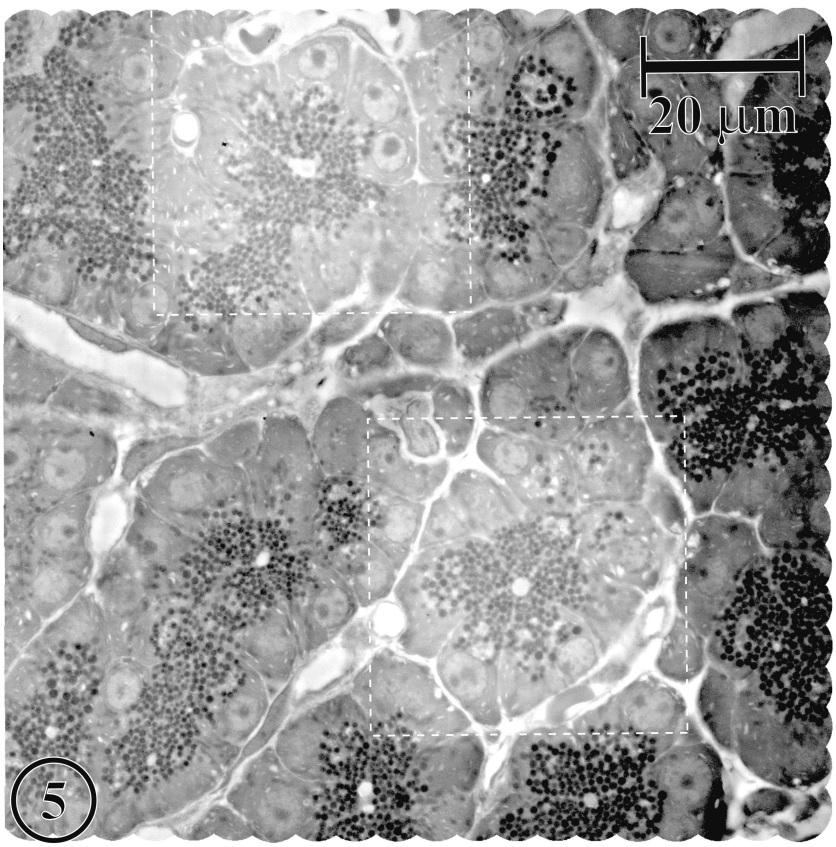

Fig. 5. An image montage at 2.4 nm wavelength, demonstrating the effect of extreme radiation dose. The two regions marked by squares surround the areas imaged in Fig. 6, and were subsequently exposed to an extreme dose of about 7×10^9 Gy prior to the acquisition of this montage. The fractional mass loss in these regions, visible as increased transmitted intensity, ranged from about 20–30%, yet despite this there is no appreciable distortion of the basic tissue architecture.

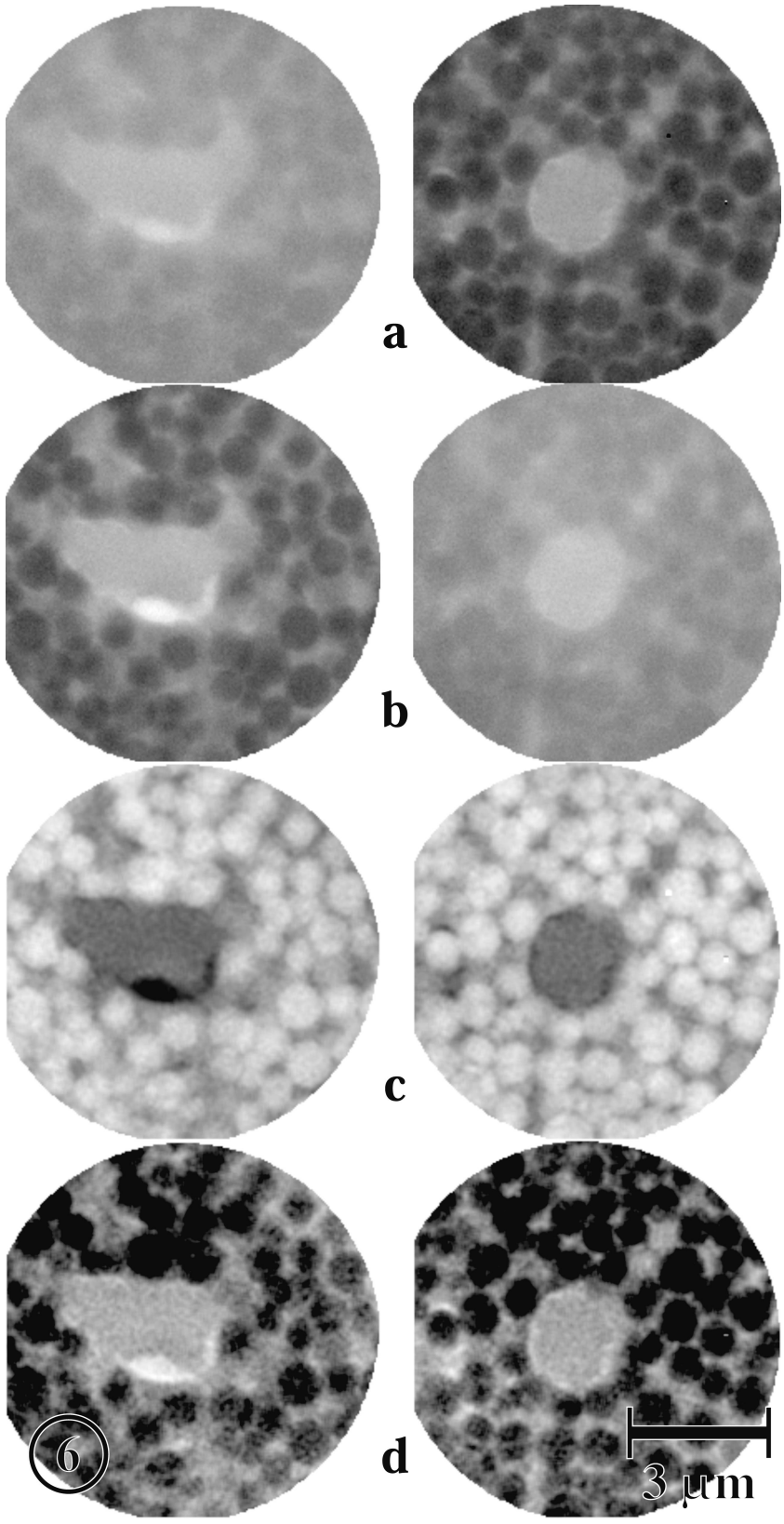

Fig. 6. Dual-wavelength imaging of the central parts of two pancreatic acini. The left column is of acinus 1, and the right is of acinus 2. (a) The first exposure of each acinus (at 3.1 nm wavelength for acinus 1, and 3.0 nm for acinus 2). (b) The second exposure (3.0 nm for acinus 1, and 3.1 nm for acinus 2). The two acini were imaged in reverse wavelength sequence from each other to control for possible radiation induced effects, as described in the text. Contrast in the transmission images is much stronger at 3.0 nm than at 3.1 nm, due to increased absorption of the nitrogen-containing tissue components on that side of the nitrogen absorption edge (see Fig. 2). (c) and (d) Calculated density maps of the protein and GMA embedding matrix components of the sample, respectively. White represents the highest density, and black the lowest.

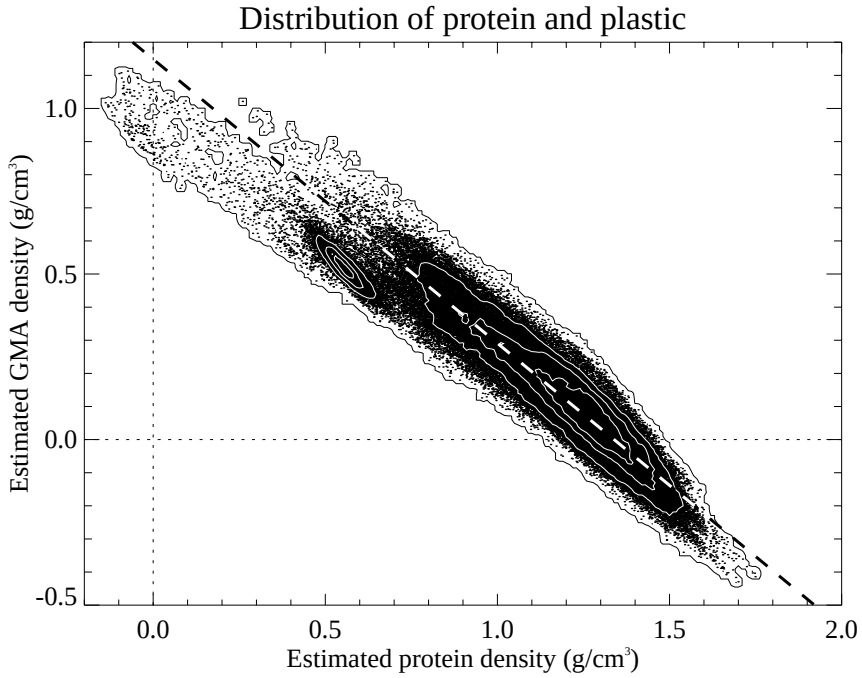

Fig. 7. A plot of GMA polymer density vs. protein density for the nearly 82 000 pixels in the areas imaged in Fig. 6. The good fit of the data to a straight line suggests that each unit of protein excludes a fixed amount of plastic embedding matrix. A second smaller peak in the data corresponds spatially to pixels in the low protein intraductal spaces, and falls below the regression line through the main peak, indicating a proportionally lower plastic content in those areas. This might be due to increased sensitivity of the plastic component to radiation in low protein areas, as indicated in Fig. 4.

polymer densities of -0.02, 0.46 and 0.51 g cm^{-3}. Figure 7 is a plot of GMA polymer density vs. protein density for each of the nearly 82 000 pixels in these two sample areas. The data fit well to a straight line of negative slope, indicating that each unit of protein excludes a fixed amount of plastic embedding matrix, essentially excluding it completely at the highest protein densities.

The regression line was fitted to points in the main peak of the scatter plot. Also apparent is a second smaller peak falling below the regression line. Spatially, the points in the second peak correspond almost exclusively to pixels in the intraductal space of the imaged acini, where the protein density was the lowest. That it falls below the regression line indicates a proportionally reduced plastic content in these areas, possibly reflecting an increased radiation sensitivity of the plastic component in low protein areas as indicated by the curves in Fig. 4. Alternatively, the ductal space may contain a chemical species with a higher fractional nitrogen content than the average protein or nucleic acid, although there is not an obvious candidate for such a species among the cell's known constituents. Also, 20% of the pixels have a calculated plastic density below zero, which is physically impossible. This is partly due to noise in the data, but it probably also results at least in part from a systematic overestimation of protein density such as that due to uncertainty in the energy calibration of the microscope as described above. A relatively small error in protein density can produce a large proportion of pixels with apparently negative plastic density because the plastic is already nearly excluded from these high protein areas.

The intercepts of the regression line indicate the density of plastic where protein density is zero, and vice versa; i.e. the densities of each component uncontaminated by the other. The y-intercept indicates a density for pure GMA of 1.15 g cm^{-3}, compared to the density of bulk GMA polymer of 1.21 g cm^{-3} (measured independently as described in the next section). Note that the latter value was used in the calculation of section thickness and thus has an impact on the density calculation: the y-intercept should therefore have this value provided the section thickness is consistent between the tissue-containing region and the pure plastic area where the thickness measurement was made. The similarity between these values supports the assumption of equal or similar thickness, and helps validate the conversion from areal to volumetric density. The x-intercept yields a protein density of 1.34 g cm^{-3} where the GMA is completely excluded by protein, essentially the same as the average density of protein in the dense centres of the zymogen granules. This is also similar to that of pure protein, about 1.4 g cm^{-3} (Sober, 1968), and suggests that protein within the granules is in the dehydrated state when the sample is prepared in this fashion.

Moreover, these intragranular protein density measurements are substantially higher than previously measured values for protein concentration in freshly isolated zymogen granules, averaging in the range 250–270 mg mL^{-1} with peak values of about 600 mg mL^{-1} (Ho & Rothman, 1983; Goncz *et al.*, 1995). The difference is probably related to major differences in sample preparation. For example, tissue shrinkage is a well known artefact of preparative treatments

such as the fixation, dehydration, and embedding used in the current work (Hanstede & Gerrits, 1983). This is manifest in measurements of zymogen granule diameter. As measured by X-ray microscopy, granules (also from fasted rats of the same strain), unfixed and in aqueous suspension, have an average diameter of 1.08 μm (Goncz *et al.*, 1995), whereas in the current work average granule diameter in GMA-embedded tissue sections (to be reported in full in a separate paper) is about 0.77 μm, consistent with electron microscopic measurements of granule size in epoxy-embedded tissue sections that have produced values in the range 0.73–0.85 μm (Ermak & Rothman, 1981; Beaudoin *et al.*, 1984). The 1.4-fold difference in linear dimension (between 1.08 and 0.77 μm), assuming it is symmetric in all dimensions, translates to a 2.8-fold difference in volume, a substantial fraction of the proportional difference of the measured densities between the two preparations: the dense centres of the zymogen granules in this study have an average density 5–5.4 times that of the average and 2.3 times that of the peak density of freshly isolated granules. This illustrates that the expression of tissue shrinkage in planar terms, typical in two-dimensional microscopy, belies the actual magnitude of volumetric shrinkage, which becomes readily apparent only with the tools to measure mass in such a direct fashion. Furthermore, the similarity of the intragranular density measured in the GMA-embedded samples to that of pure protein suggests that the mechanism of shrinkage is related to dehydration of the sample with incomplete replacement of water by the embedding matrix.

Although other investigators have used dual- and multi-wavelength imaging at the carbon K-shell and calcium L-shell absorption edges to obtain contrast and map tissue components (Kenney *et al.*, 1985; Zhang *et al.*, 1996; Buckley *et al.*, 1998), this is the first work to use dual-wavelength imaging at the nitrogen K-shell edge in a high resolution X-ray optical microscope. Using an X-ray contact microradiographic system, Ito *et al.* (1996) were able to obtain spectromicrographs of cultured cells across a large part of the soft X-ray spectrum (including the nitrogen edge) at a resolution comparable to that of a visible light microscope. Nitrogen-based imaging, in addition to taking advantage of the large nitrogen difference between tissue and embedding medium, can also in principle be used to differentiate protein from DNA by exploiting a strong difference between the absorption peaks in their nitrogen near-edge spectra (Kirtley *et al.*, 1992; Shinohara *et al.*, 1998). This has been done at the carbon edge by Zhang *et al.* (1996).

Section thickness

Because of the well-defined relationship between transmission and the areal density of the sample (see Eq. (1b)), it is possible to determine the thickness of a sample given its density and mass-dependent absorption coefficient. Rectangular blocks of polymerized GMA embedding material were machined, measured and weighed (courtesy of W. A. Bates and W. Meyer-Ilse, Lawrence Berkeley National Laboratory) to determine the density of the plastic: 1.21 g cm^{-3}. The transmission of seven sections, normalized to the transmission through the silicon nitride support membrane on each of their respective sample holders, was measured at three to six spots on each section (24 total) in areas containing only the plastic (devoid of tissue) to determine their thickness.

The nominal microtome setting for thickness was 0.75 μm. The actual thickness calculated as described ranged from 0.31 to 0.91 μm over these seven sections, with an average thickness of 0.56 μm and a standard deviation of 0.23 μm. However, thickness variation within sections, as measured by the standard deviation from the respective mean values, was only 0.02 μm. These measurements are consistent with the finding of Helander (1983) that thickness within sections is quite uniform, particularly in the pure plastic component.

Conclusions

While X-ray microscopic instrumentation has matured in recent years, corresponding sample preparation methods are still in their infancy. This work demonstrates that GMA embedding and sectioning, widely used in other forms of microscopy, is applicable to X-ray microscopy essentially without modification. This should allow soft X-ray microimaging, with its unique contrast properties, of a wide range of tissues prepared routinely as for other forms of microscopy, including pathology samples. It also offers the opportunity to carry out multimodal microscopy (including visible light, X-ray, and electron imaging) on a given sample. This could be a powerful approach because the information provided by X-ray microscopy complements that provided by visible light and electron microscopies. In addition, because one surface of the sample can be left exposed, scanned probe microscopy (e.g. atomic force microscopy or scanning tunnelling microscopy) can also be performed. For example, we have recently begun measurements to assess more accurately the uniformity of the section thickness by AFM.

As shown, good contrast is obtained between the sample and the embedding medium due to the variable nitrogen content of the tissue. This also makes it possible, using two or more imaging wavelengths, to obtain chemically specific contrast near the nitrogen absorption edge. Furthermore, one can similarly take advantage of the near-edge absorption structure of any other major elemental constituent in the sample, including carbon, oxygen, and minerals such as calcium (Kirtley *et al.*, 1992; Zhang *et al.*, 1996; Buckley *et al.*, 1998).

Radiation-induced changes in the sample, such as mass loss and distortion, especially shrinkage, have been a major obstacle in X-ray microscopy, particularly with respect to specialized methods that require multiple exposures. The samples prepared as described here demonstrated good radiation tolerance at the doses used for imaging, with little mass loss and no appreciable distortion. With some additional measures to reduce dose and prevent mass loss, a range of powerful X-ray microscopic imaging modes becomes practical. For example, in a typical XM-1 configuration at the time of this study (with its attendant sources of optical inefficiency) it took about 10^7 Gy to form an image, about three times less than the dose that produced significant (5%) mass loss in GMA-embedded tissue sections. This is also about the same as the theoretical dose required to do soft X-ray microtomography with 80 nm resolution in all three dimensions (Loo & Rothman, 1995; Loo & Rothman, 1997). Thus far, three-dimensional imaging has been possible only when the number of views is small, as in stereoscopy (Loo *et al.*, 1992a; Loo *et al.*, 1992b), or when full microtomography is combined with cryofixation of the sample to prevent radiation-induced changes (Weiß *et al.*, 2000). The sample preparation method presented here should substantially broaden the types of samples on which quantitative, high-resolution three-dimensional elemental mapping can be performed. Similarly, chemical mapping by spectromicroscopy with high spectral resolution, requiring many exposures at different wavelengths, is feasible. Finally, because these samples are insensitive to radiation-induced distortion, they are highly amenable to montage imaging and large-field survey studies of tissue (Loo *et al.*, 2000).

Acknowledgements

We wish to thank our colleagues at the Center for X-ray Optics, Advanced Light Source, and Life Sciences Division at Lawrence Berkeley National Laboratory, at Lawrence Livermore National Laboratory, at the University of California, San Francisco, Berkeley, and Davis, at the State University of New York, Stony Brook, and at Genteric Corporation for their help in this work. We are grateful in particular to the following individuals, who have made critical contributions: David T. Attwood, Mary Helen Barcellos-Hoff, William A. Bates, John T. Brown, Daniel E. Callahan, Je-Wei Chen, Dino R. Ciarlo, Nusi P. Dekker, Gregory P. Denbeaux, Everett H. Harvey, Theresa Hashim, Catherine A. Hong, Malcolm R. Howells, Yongfeng Hu, Chris J. Jacobsen, Melvin P. Klein, Carolyn A. Larabell, Aaron J. Lee, Jesse Lee, Betty A. Maddux, Bonnie J. McClintock, Werner Meyer-Ilse, Mario M. Moronne, Daniel M. Pinkas, Jos Polman, Shradda A. Ravani, Joseph A. Regezi, Paula Sicurello, Joachim Stohr, Hsien-Chen Tseng, Elise Y. Tung-Loo, and Brian Yates. We especially thank the late Werner Meyer-Ilse and his staff for generously providing the use of and continually improving the XM-1 microscope facility, and for many helpful discussions and comments. B.W.L. gratefully acknowledges the support of a National Institutes of Health training grant to the UCSF/UCB Bioengineering Graduate Group, a Laboratory Graduate fellowship from Associated Western Universities, Inc., and a fellowship from the Regents of the University of California. The research of A.P.H. is funded in part by a strategic project grant from NSERC (Canada). CSRF is funded by NSERC to operate at the Synchrotron Radiation Center, University of Wisconsin, Madison, which is supported by National Science Foundation grant DMR 95–31009. The XM-1 project and the ALS are supported by the U.S. Department of Energy, Office of Basic Energy Sciences and Office of Biological and Environmental Research, and the Laboratory Directed Research and Development Program of the E. O. Lawrence Berkeley National Laboratory, under the Department of Energy contract No. DE-AC03-76SF00098.

References

Ade, H., Smith, A.P., Zhang, H., Zhuang, G.R., Kirz, J., Rightor, E. & Hitchcock, A. (1997) X-ray spectromicroscopy of polymers and tribological surfaces at beamline X1A at the NSLS. *J. Electron Spect. Rel. Phenom.* **84**, 53–71.

Anderson, E.H. (2000) Zone plate fabrication with the Nanowriter. *X-Ray Microscopy: Proceedings of the VI International Conference on X-ray Microscopy, Berkley, August 2-6, 1999* (ed. by W. Meyer-Ilse, T. Warwick and D. T. Attwood), AIP Conference Proceedings **507**. American Institute of Physics, College Park.

Anderson, E.H. & Kern, D. (1992) Nanofabrication of zone plates for x-ray microscopy. *X-Ray Microscopy III: Proceedings of the Third International Conference, London, September 3–7, 1990* (ed. by A. G. Michette, G. R. Morrison and C. J. Buckley), pp. 75–78. Springer-Verlag, Berlin.

Beaudoin, A.R., Grondin, G., Filion, M. & Lord, A. (1984) Secretagogues cause a preferential discharge of large size granules in rat pancreas. *Can J. Biochem. Cell Biol.* **62**, 1288–1292.

Beckstead, J.H., Halverson, P.S., Ries, C.A. & Bainton, D.F. (1981) Enzyme histochemistry and immunohistochemistry on biopsy specimens of pathologic human bone marrow. *Blood*, **57**, 1088–1098.

Bennett, H.S., Wyrick, A.D., Lee, S.W. & McNeil, J.H. Jr (1976) Science and art in preparing tissues embedded in plastic for light microscopy, with special reference to glycol methacrylate, glass knives and simple stains. *Stain Technol.* **51**, 71–97.

Brinn, N.T. & Pickett, J.P. (1979) Glycol methacrylate for routine, special stains, histochemistry, enzyme histochemistry and immunohistochemistry: a simplified cold method for surgical biopsy tissue. *J. Histotechnol.* **2**, 125–130.

Buckley, C.J., Khaleque, N.I., Bellamy, S.J., Robins, M. & Zhang, X. (1998) Mapping the organic and inorganic components of bone. *X-Ray Microscopy and Spectromicroscopy: Proceedings of the Fifth International Conference, Würzburg, August 19–23, 1996* (ed. by J.

Thieme, G. Schmahl, D. Rudolph and E. Umbach), pp. II–47–II-55. Springer, Berlin.

Chen, C.T., Ma, Y. & Sette, F. (1989) K-shell photoabsorption of the N_2 molecule. *Phys Rev. A (General Physics)*, **40**, 6737–6740.

Cole, M.B. Jr & Sykes, S.M. (1974) Glycol methacrylate in light microscopy: a routine method for embedding and sectioning animal tissues. *Stain Technol.* **49**, 387–400.

Ermak, T.H. & Rothman, S.S. (1981) Zymogen granules of pancreas decrease in size in response to feeding. *Cell Tissue Res.* **214**, 51–66.

Goncz, K.K., Behrsing, R. & Rothman, S.S. (1995) The protein content and morphogenesis of zymogen granules. *Cell Tissue Res.* **280**, 519–530.

Hanstede, J.G. & Gerrits, P.O. (1983) The effects of embedding in water-soluble plastics on the final dimensions of liver sections. *J. Microsc.* **131**, 79–86.

Heck, J.M., Attwood, D.T., Meyer-Ilse, W. & Anderson, E.H. (1999) Resolution determination in X-ray microscopy: an analysis of the effects of partial coherence and illumination spectrum. *J. X-Ray Sci. Technol.* **8**, 95–104.

Helander, K.G. (1983) Thickness variations within individual paraffin and glycol methacrylate sections. *J. Microsc.* **132**, 223–227.

Henke, B.L., Gullikson, E.M. & Davis, J.C. (1993) X–ray interactions: photoabsorption, scattering, transmission, and reflection at E=50–30000 eV, Z=1–92. *Atomic Data Nuclear Data Tables*, **54**, 181–342.

Hitchcock, A.P. & Mancini, D.C. (1994) Bibliography and database of inner shell excitation spectra of gas phase atoms and molecules. *J. Electron Spect. Rel. Phenom.* **67**, 1–132.

Hitchcock, A.P., Tyliszczak, T., Heng, Y.M., Cornelius, R., Brash, J.L., Ade, H., Anders, S., Scholl, A. & Nolting, F. (2000) X-ray spectromicroscopy studies of protein–polymer interactions. *X-Ray Microscopy: Proceedings of the VI International Conference on X-Ray Microscopy, Berkeley, August 2–6, 1999* (ed. by W. Meyer-Ilse, T. Warwick and D. T. Attwood), pp. 235–238. AIP Conference Proceedings 507. American Institute of Physics, College Park.

Ho, J.J.L. & Rothman, S.S. (1983) Protein concentration in the pancreatic zymogen granule. *Biochim. Biophys. Acta*, **755**, 457–466.

Irtel von Brenndorff, A., Moronne, M.M., Larabell, C., Selvin, P. & Meyer-Ilse, W. (1994) Soft X-ray stimulated high resolution luminescence microscopy. *X-Ray Microscopy IV: Proceedings of the Fourth International Conference, Chernogolovka, Russia, September 20–24, 1993* (ed. by V. V. Aristov and A. I. Erko). Bogorodskii Pechatnik, Chernogolovka.

Ito, A., Shinohara, K. & Kitajima, Y. (2000) XANES of mammalian cells in the soft X-ray region for the basis of X-ray imaging. *X-Ray Microscopy: Proceedings of the VI International Conference on X-ray Microscopy, Berkeley, August 2–6, 1999* (ed. by W. Meyer-Ilse, T. Warwick and D. T. Attwood), pp. 145–148. AIP Conference Proceedings 507. American Institute of Physics, College Park.

Ito, A., Shinohara, K., Nakano, H., Matsumura, T. & Kinoshita, K. (1996) Measurement of soft X-ray absorption spectra and elemental analysis in local regions of mammalian cells using an electronic zooming tube. *J. Microsc.* **181**, 54–60.

Kenney, J.M., Jacobsen, C., Kirz, J., Rarback, H., Cinotti, F., Thomlinson, W., Rosser, R. & Schidlovsky, G. (1985) Absorption microanalysis with a scanning soft X-ray microscope: mapping the distribution of calcium in bone. *J. Microsc.* **138**, 321–328.

Khaleque, N.I. & Buckley, C.J. (1998) Image contrast in embedded specimens using NEXAFS spectroscopy. *X-Ray Microscopy and Spectromicroscopy: Proceedings of the Fifth International Conference, Würzburg, August 19–23, 1996* (ed. by J. Thieme, G. Schmahl, D. Rudolph and E. Umbach), pp. III–95–III-98. Springer, Berlin.

Kirtley, S.M., Mullins, O.C., Chen, J., van Elp, J., George, S.J., Chen, C.T., O'Halloran, T. & Cramer, S.P. (1992) Nitrogen chemical structure in DNA and related molecules by X-ray absorption spectroscopy. *Biochim. Biophys. Acta* **1132**, 249–254.

Kirz, J., Jacobsen, C. & Howells, M. (1995) Soft x-ray microscopes and their biological applications. *Q. Rev. Biophys.* **28**, 33–130.

Larabell, C.A., Yager, D. & Meyer-Ilse, W. (2000) Localization of proteins and nucleic acids using soft X-ray microscopy. *X-Ray Microscopy: Proceedings of the VI International Conference on X-ray Microscopy, Berkeley, August 2–6, 1999* (ed. by W. Meyer-Ilse, T. Warwick and D. T. Attwood), pp. 107–112. AIP Conference Proceedings 507. American Institute of Physics, College Park.

Leapman, R.D. & Andrews, S.B. (1991) Biological electron energy loss spectroscopy: the present and the future. *Microsc. Microanal. Microstruct.* **2**, 387–394.

Loo, B.W. Jr, Meyer-Ilse, W. & Rothman, S.S. (2000) Automatic image acquisition, calibration, and montage assembly for biological X-ray microscopy. *J. Microsc.* **197**, 185–201.

Loo, B.W. Jr, Parvin, B. & Rothman, S.S. (1996) Two- and three-dimensional segmentation for measurement of particles in the analysis of microscopic digital images of biological samples. *Three-Dimensional Microscopy: Image Acquisition and Processing III, San Jose, California, January 30 – February 1, 1996* (ed. by C. J. Cogswell, G. S. Kino and T. Wilson). Proceedings SPIE, **2655**, 209–215.

Loo, B.W. Jr & Rothman, S.S. (1995) High resolution microscopic imaging with x-rays: technology and application to the biological sciences. *Proceedings of WESCON'95, San Francisco, California, November 7–9 1995*, pp. 668–672.

Loo, B.W. Jr & Rothman, S.S. (1997) High resolution X-ray microtomography of biological samples: requirements and strategies for satisfying them. *Proceedings of the Workshop on High Resolution Computed Microtomography, Ernest Orlando Lawrence Berkeley National Laboratory, University of California, August 12–13, 1996* (ed. by E. Schlueter and F. Schlacter), pp. 223–262. U.S. Department of Energy, Berkeley, CA

Loo, B.W. Jr, Williams, S., Lin, W.T., Love, W.H., Meizel, S. & Rothman, S.S. (1992a) High resolution X-ray stereomicroscopy: true three-dimensional imaging of biological samples. *Soft X-Ray Microscopy, San Diego, CA, USA, July 19–21, 1992. Proc. SPIE*, **1741**, 393–401.

Loo, B.W. Jr, Williams, S., Meizel, S. & Rothman, S.S. (1992b) X-ray stereomicroscopy: high resolution 3-D imaging of human spermatozoa in aqueous suspension with natural contrast. *J. Microsc.* **166**, RP5–RP6.

Maser, J., Jacobsen, C., Kirz, J., Osanna, A., Spector, S., Wang, S. &

Warnking, J. (1998) Development of a cryo scanning transmission x-ray microscope at the NSLS. *X-Ray Microscopy and Spectromicroscopy: Proceedings of the Fifth International Conference, Würzburg, August 19–23, 1996* (ed, by J. Thieme, G. Schmahl, D. Rudolph and E. Umbach), pp. I–35–I-44. Springer, Berlin

Meyer-Ilse, W., Denbeaux, G., Johnson, L.E., Bates, W., Lucero, A. & Anderson, E. (2000) The high resolution X-ray microscope, XM-1. *X-Ray Microscopy: Proceedings of the VI International Conference on X-ray Microscopy, Berkeley, August 2–6, 1999* (ed. by W. Meyer-Ilse, T. Warwick and D. T. Attwood), pp. 129–134. AIP Conference Proceedings 507. American Institute of Physics, College Park.

Meyer-Ilse, W., Medecki, H., Brown, J.T., Heck, J.M., Anderson, E.H., Stead, A., Ford, T., Balhorn, R., Petersen, C., Magowan, C. & Attwood, D.T. (1998) X-ray microscopy in Berkeley. *X-Ray Microscopy and Spectromicroscopy: Proceedings of the Fifth International Conference, Würzburg, August 19–23, 1996* (ed. by J. Thieme, G. Schmahl, D. Rudolph and E. Umbach), pp. I–1–I-12. Springer, Berlin.

Meyer-Ilse, W., Medecki, H., Jochum, L., Anderson, E., Attwood, D., Magowan, C., Balhorn, R., Moronne, M., Rudolph, D. & Schmahl, G. (1995) New high-resolution zone-plate microscope at Beamline 6.1 of the ALS. *Synchrotron Radiation News*, **8**, 29–33.

Moronne, M.M. (1999) Development of X-ray excitable luminescent probes for scanning x-ray microscopy. *Ultramicroscopy*, **77**, 23–36.

Niemann, B., Rudolph, D. & Schmahl, G. (1983) The Göttingen x-ray microscopes. *Nucl. Instrum. Meth.* **208**, 367–371.

Nyakatura, G., Meyer-Ilse, W., Guttmann, P., Niemann, B., Rudolph, D., Schmahl, G., Sarafis, V., Hertel, N., Uggerhøj, E., Skriver, E., Nørgaard, J.O.R. & Maunsbach, A.B. (1988) Investigations of biological specimens with the x-ray microscope at BESSY. *X-Ray Microscopy II: Proceedings of the Second International Symposium, Brookhaven, New York, August 31 – September 4, 1987* (ed. by D. Sayre, M. R. Howells, J. Kirz and H. Rarback), pp. 365–371. Springer-Verlag, Berlin.

Pearse, A.G.E. (1985) Biogenic amines. *Histochemistry: Theoretical and Applied*, 4th edn. Churchill Livingstone, Edinburgh.

Rightor, E.G., Hitchcock, A.P., Ade, H., Leapman, R.D., Urquhart, S.G., Smith, A.P., Mitchell, G., Fischer, D., Shin, H.J. & Warwick, T. (1997) Spectromicroscopy of poly (ethylene terephthalate): comparison of spectra and radiation damage rates in X-ray absorption and electron energy loss. *J. Phys. Chem. B.* **101**, 1950–1960.

Rothman, S., Anderson, E., Attwood, D., Batson, P., Buckley, C., Goncz, K., Howells, M., Jacobsen, C., Kern, D., Kirz, J., Rarback, H., Rivers, M., Shu, D., Tackaberry, R. & Turek, S. (1990) Soft X-ray microscopy in biology and medicine: status and prospects. *Physica Scripta* **T31**, 18–22.

Rothman, S.S., Goncz, K.K. & Loo, B.W. Jr (1992) Following protein transport with the high resolution X-ray microscope. *X-Ray Microscopy III: Proceedings of the Third International Conference, London, September 3–7, 1990* (ed. by A. G. Michette, G. R. Morrison and C. J. Buckley), pp. 373–383. Springer-Verlag, Berlin.

Schmahl, G., Rudolph, D., Niemann, B. & Christ, O. (1980) Zone-plate x-ray microscopy. *Q. Rev. Biophysics*. **13**, 297–315.

Schmahl, G., Rudolph, D., Schneider, G., Thieme. J., Schliebe, T., Kaulich, B. & Hettwer (1996) Diffraction optics for X-ray imaging. *Microelect. Eng.* **32**, 351–367.

Schneider, G. & Niemann, B. (1998) Cryo X-ray microscopy experiments with the X-ray microscope at BESSY. *X-Ray Microscopy and Spectromicroscopy: Proceedings of the Fifth International Conference, Würzburg, August 19–23, 1996* (ed. by J. Thieme, G. Schmahl, D. Rudolph and E. Umbach), pp. I–25–I-34. Springer, Berlin.

Shinohara, K., Ito, A. & Kobayashi, K. (1998) Measurement of XANES spectra of biological molecules in the soft x-ray region. *X-Ray Microscopy and Spectromicroscopy: Proceedings of the Fifth International Conference, Würzburg, August 19–23, 1996* (ed. by J. Thieme, G. Schmahl, D. Rudolph and E. Umbach), pp. III–157–III-161. Springer, Berlin.

Sober, H.A., ed. (1968) *CRC Handbook of Biochemistry:. Selected Data for Molecular Biology.* Chemical Rubber Company, Cleveland.

Warwick, T., Franck, K., Kortright, J.B., Meigs, G., Moronne, M., Myneni, S., Rotenberg, E., Seal, S., Steele, W.F., Ade, H., Garcia, A., Cerasari, S., Denlinger, J., Hayakawa, S., Hitchcock, A.P., Tyliszczak, T., Kikuma, J., Rightor, E.G., Shin, H.J. & Tonner, B.P. (1998) A scanning transmission X-ray microscope for materials science spectromicroscopy at the Advanced Light Source. *Rev. Sci. Instrum.* **69**, 2964–2973.

Weiß, D., Peuker, M. & Schneider, G. (1998) Radiation-enhanced network formation in copolymer galvanoforms for diffractive nickel X-ray optics with high aspect ratios. *Appl. Phys. Lett.* **72**, 1805–1807.

Weiß, D., Schneider, G., Niemann, B., Guttmann, P., Rudolph, D. & Schmahl, G. (2000) Tomographic imaging of cryogenic biological specimens with the x-ray microscope at BESSY. *X-Ray Microscopy: Proceedings of the VI International Conference on X-ray Microscopy, Berkeley, August 2–6, 1999* (eds W. Meyer-Ilse, T. Warwick and D. T. Attwood), pp. 123–128. AIP Conference Proceedings 507. American Institute of Physics, College Park.

Wilhein, T., Rothweiler, D., Tusche, A., Scholze, F. & Meyer-Ilse, W. (1994) Thinned, back-illuminated CCDs for x-ray microscopy. *X-Ray Microscopy IV: Proceedings of the Fourth International Conference, Chernogolovka, Russia, September 20–24, 1993* (ed. by V. V. Aristov and A. I. Erko), pp. 470–474. Bogorodskii Pechatnik, Chernogolovka.

Yates, B.W., Hu. Y.F., Tan, K.H., Retzlaff, G., Cavell, R.G., Sham, T.K. & Bancroft, G.M. (2000) First results from the Canadian SGM beamline at SRC. *J. Synchrotron Radiation*, **7**, 296–300.

Zhang, X., Balhorn, R., Mazrimas, J. & Kirz, J. (1996) Mapping and measuring DNA to protein ratios in mammalian sperm head by XANES imaging. *J. Struct. Biol.* **116**, 335–344.